

## Evolution of enhanced magmatism at the ultraslow spreading Southwest Indian Ridge between 46°E and 53.5°E

Jie Chen<sup>a,b</sup>, Tao Zhang<sup>a, \*\*</sup>, Huaiming Li<sup>a</sup>, Chunhui Tao<sup>a,c,\*</sup>, Mathilde Cannat<sup>b</sup>, Daniel Sauter<sup>d</sup>

<sup>a</sup> Key Laboratory of Submarine Geosciences, Second Institute of Oceanography, MNR, Hangzhou, China

<sup>b</sup> Université Paris Cité, Institut de Physique du Globe de Paris, CNRS, Paris, France

<sup>c</sup> School of Oceanography, Shanghai Jiao Tong University, Shanghai, China

<sup>d</sup> Institut Terre et Environnement de Strasbourg ITES, Université de Strasbourg, CNRS UMR 7063, Strasbourg, France

### ARTICLE INFO

#### Keywords:

Ultraslow spreading Southwest Indian Ridge  
Enhanced magmatism  
Seafloor spreading mode  
Ridge segmentation  
Bathymetry  
Gravity

### ABSTRACT

The Indomed-Gallieni supersegment (46–52°E) of the Southwest Indian Ridge (SWIR) has been of interest as a melt-rich endmember of ultraslow spreading mid-ocean ridges, attributed to enhanced magmatism since 11 Ma. This provides an excellent opportunity to study the evolution and the impact of enhanced magmatism at mid-ocean ridges. Here we combine shipboard bathymetry and gravity data over the SWIR 46–53.5°E. We illustrate that the enhanced magmatism initiated in the western part of the Indomed-Gallieni supersegment with decreasing crustal production and no propagation. In the eastern part, the enhanced magmatism propagated to the east at decreasing propagating velocities, producing an increasingly thick crust. The present propagation tip is at 51.9°E, ~30 km to the west of the Gallieni transform fault (TF). The most magmatically-robust area of the propagation has been located near 50.5°E since ~6 Ma. We hypothesize that a mantle melting anomaly with heterogeneous upwelling rates and/or geometry was responsible for the change of the enhanced magmatism. The enhanced magmatism plays significant roles in ridge segmentation and seafloor spreading modes. The degree of along-axis melt focusing was lowered, causing the segmentation to be typical of slow spreading ridges. As magmatism dramatically decreases over 160 km along the ridge axis from the most robust (producing a 9.5-km-thick crust at 50.5°E) to nearly-amagmatic near the Gallieni TF, this ridge section exhibits the full spectrum of ultraslow spreading modes, changing from magmatically-controlled (intense volcanism and almost no faulting) to tectonically-dominated (smooth ridges and extensive peridotites outcrops) modes.

### 1. Introduction

The Mid-Ocean Ridge (MOR) is the birthplace of the oceanic lithosphere that covers 65% of the Earth's surface, through seafloor spreading with magmatic and tectonic extension, which is mainly controlled by spreading rate and melt supply (Buck et al., 2005; Cannat et al., 2019; Phipps Morgan and Chen, 1993). Ultraslow spreading ridges (full spreading rate of <20 km/Ma), which account for ~20% of the global MOR, are believed to have sparse magmatism with extensive tectonic extension (Cannat et al., 2006; Dick et al., 2003; Minshull et al., 2006). However, recent studies show intensive magmatism at several ultraslow spreading ridge sections (Li et al., 2015; Michael et al., 2003; Sauter et al., 2009), suggesting a more diverse, not overall lower, melt supply relative to faster spreading ridges. Such axial melt distribution

has been documented to vary on regional (Cannat et al., 2008; Georgan et al., 2001; Michael et al., 2003) and segment (Cannat et al., 1999a; Grindlay et al., 1998; Sauter et al., 2001; Zhang et al., 2018) scales, controlling magmatic and tectonic processes as well as ridge segmentation (Carbotte et al., 2015).

On the regional scale (>200 km), ridge sections at ultraslow spreading ridges with a poor melt supply, such as the easternmost Southwest Indian Ridge (SWIR) (Cannat et al., 2006; Sauter et al., 2013) and the Sparsely Magmatic Zone of the Gakkel Ridge (Cochran et al., 2003; Michael et al., 2003) are characterized by an overall deep axial valley with extensive mantle peridotites exhumed on the seafloor, thin (or missing) magmatic crusts, and high Mantle Bouguer gravity Anomalies (MBAs). In contrast, melt supply can be regionally rich, producing thick magmatic crusts and displaying a relatively shallow (or free) axial

\* Corresponding author at: Key Laboratory of Submarine Geosciences, Second Institute of Oceanography, MNR, Hangzhou, China.

\*\* Corresponding author.

E-mail addresses: [tao\\_zhang@sio.org.cn](mailto:tao_zhang@sio.org.cn) (T. Zhang), [taochunhuimail@163.com](mailto:taochunhuimail@163.com) (C. Tao).

valley and low MBAs, such as the Indomed-Gallieni supersegment of the SWIR (Li et al., 2015; Sauter et al., 2009; Yu and Dick, 2020). This regional-scale variation of melt supply may be attributed to the heterogeneities of the thermal structure and/or mantle composition, e.g., a melt-rich region corresponding to a high mantle temperature and/or a high volatile (e.g., water) content (Asimow and Langmuir, 2003; Cannat et al., 2008; Michael et al., 2003; Robinson et al., 2001).

On the segment scale (<100 km), segment centers receive more melt than their corresponding segment ends near transform faults (TFs) or nontransform discontinuities (NTD) (Cannat et al., 1999b; Li et al., 2015; Sauter et al., 2001), similar to what has been observed at the slow spreading Mid-Atlantic Ridge (MAR) (Lin et al., 1990). Such along-axis melt focusing results in a topographic high, a thickened crust, and a low MBA at the segment center (Li et al., 2015; Sauter et al., 2001), where volcanic seafloor is almost symmetrically accreted from an axial volcanic ridge (AVR) with high-angle normal faults (Mendel et al., 2003). While at segment ends or some melt-poor segments, reduced melt supply leads to different spreading modes, in which one or even two (in case of nearly zero melt supply) plates are accommodated by long-offset (up to 10 km), low-angle detachment faults that exhume gabbros and peridotites on the seafloor (Cannat et al., 2019; Sauter et al., 2013; Zhou et al., 2022).

In this paper, we focus on the ultraslow spreading SWIR 46–53.5°E (full spreading rate of 14 km/Ma), including the melt-rich Indomed-Gallieni supersegment (580 km long) and the melt-poor Gallieni-Gazelle segment (93 km long) named by their bounding TFs (Fig. 1a). The Indomed-Gallieni supersegment presents a higher melt supply than its adjacent ridge sections, its older flanks, and the SWIR average (Sauter et al., 2009), including the most magmatically-robust endmember at 50.5°E (9.5-km thick crust) among ultraslow spreading ridges (Chen et al., 2021; Jian et al., 2017; Li et al., 2015; Niu et al., 2015). This regional high melt supply has been depicted as a domain with elevated seafloor and reduced MBAs (identified in Fig. 1), which may originate from a melting anomaly event starting 11 Ma ago with a V-shaped, eastward propagation (Sauter et al., 2009). In contrast, the Gallieni-Gazelle segment has widespread peridotites exposed on the seafloor, corresponding to a thin or missing magmatic crust (Zhou and Dick, 2013).

The SWIR 46–53.5°E, with the characteristic of a highly variable melt supply in time and space, therefore, provides an excellent opportunity to address several long-standing questions for ultraslow spreading ridges. If melt supply increases with time, what is the possible mechanism? What is the spectrum of melt supply at ultraslow spreading ridges, and how does it link with ridge segmentation, faulting patterns, and seafloor

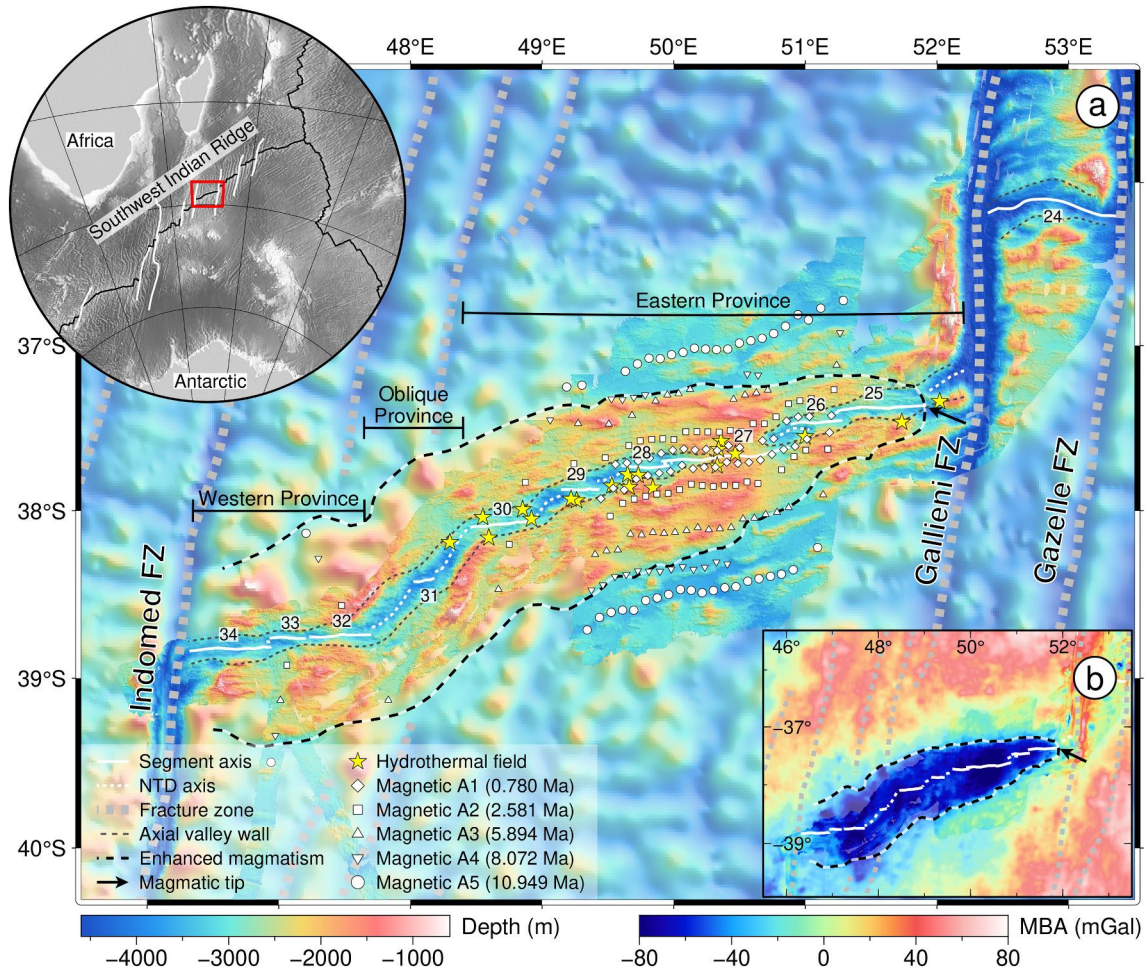


**Fig. 1.** Bathymetry and MBA maps at the SWIR between 45.5°E and 53.5°E. (a) The shipboard bathymetry data (Li et al., 2020; Liu et al., 2020; Sauter et al., 2009; Zhou and Dick, 2013) were superimposed on the GEBCO 1 min grid (Weatherall et al., 2015). 3 provinces (Eastern, Oblique, and Western) and 11 segments (#24–#34) are labeled. Yellow stars mark the locations of hydrothermal fields (Huang et al., 2021; Li et al., 2020; Tao et al., 2012). See legends for symbols and magnetic picks A1–A5 (Sauter et al., 2009). The boundary of the enhanced magmatism is drawn by a suddenly elevated seafloor (Fig. 1a) and reduced MBAs (Fig. 1b). The arrow (near the Gallieni TF) indicates the tip of the eastward propagation of the enhanced magmatism. The inset shows the location of the SWIR and the study area inside the red square. (b) MBA map calculated by shipboard bathymetry and gravity data (bright colors) filled with satellite-derived data (light colors). (For interpretation of the references to colour in this figure legend, the reader is referred to the web version of this article.)

spreading modes? Here we combined shipboard bathymetry and gravity data along the SWIR 46–53.5°E (Figs. 1 and 2), collected during the annual Chinese DY cruises between 2008 and 2016 (Li et al., 2020; Liu et al., 2020) with data collected during the French cruises in the 1990s (Sauter et al., 2009). The combined datasets allow us to 1) examine the variation of melt supply within the SWIR 46–53.5°E, 2) illustrate spatial and temporal evolution of the enhanced magmatism and explore its impact, and 3) investigate the spectrum of melt supply at an ultraslow spreading rate and its related faulting pattern and seafloor spreading modes.

## 2. Data and methods

The whole shipboard bathymetry and gravity dataset cover 40–220 km off-axis seafloor along the SWIR between 46°E and 53.5°E. The later

dataset was acquired during the Chinese DY cruises, including the DY115-20 Legs 5–7 in 2008–2009, DY115-21 Legs 5–7 in 2009–2010, DY125-30 Legs 1–4 in 2013–2014, DY125-34 Legs 1–4 in 2014–2015, and DY125-39 Legs 1–4 in 2015–2016 aboard the R/V Dayang Yihao and DY125-40 Legs 1–4 in 2015–2016 aboard the R/V Xiangyanghong 10. The earlier dataset was acquired during the French Gallieni and SWIFT cruises in the 1990s (Sauter et al., 2009). Two datasets have an excellent agreement in the overlapping area.

### 2.1. Bathymetry data

The later bathymetry data were collected using the Simrad EM120 multibeam system on the R/V Dayang Yihao and the SeaBeam 3012 multibeam system on the R/V Xiangyanghong 10 (Li et al., 2020; Liu et al., 2020; Zhou and Dick, 2013). We combined the bathymetry data

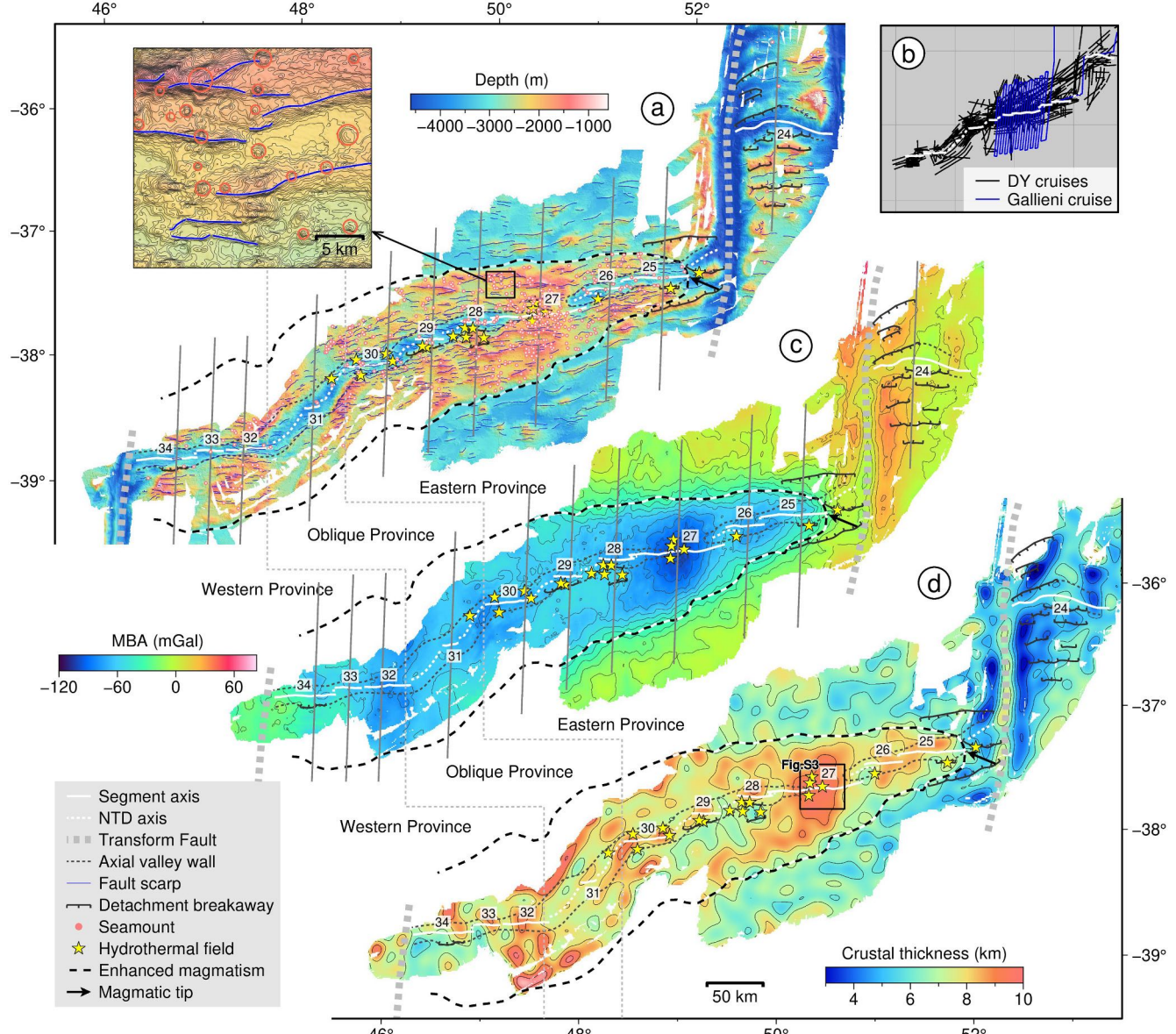


**Fig. 2.** Geological mapping and gravity inversion. (a) Geological interpretation superimposed on the bathymetry map (see legend for symbols). Across-axis profiles are shown in Fig. 3. The inset shows examples of picking seamounts and faults. (b) Gravity survey tracks of the DY cruises (black lines) and the Gallieni cruise (blue lines). (c) MBA map calculated by subtracting the predicted gravity effect based on shipboard bathymetry and a 6 km-thick model crust from the FAA in Fig. S2b. The grid spacing of the FAA and MBA maps is 0.5 min. (d) Crustal thickness, calibrating the center of segment #27 (50.5°E) to 9.5 km, which is defined by depths to the Moho interfaces (Jian et al., 2017; Li et al., 2015). Black square shows the location in Fig. 7. (For interpretation of the references to colour in this figure legend, the reader is referred to the web version of this article.)

into a grid interval of 100 m (Figs. 1a and 2a). Faults and seamounts are manually detected. The obtained features (see examples in the inset of Fig. 2a) were manually checked and digitized with seafloor topography, slope, and roughness maps (Fig. 2a, S1a, and S1b, respectively). Fault density was calculated as kernel density with a grid size of 110 m and a search radius of 10 km (Fig. S1c). Subsidence curves, seafloor deepening with age due to the plate cooling, were predicted using a simple law of the square root of spreading age ( $T$ ) and the empirical depth ( $D$ ) (Parsons and Sclater, 1977):  $D(T) = 340 T^{0.5} + D(T=0)$ , and assuming symmetrical spreading around the location of the present-day ( $T=0$ ) ridge axis (Fig. 3).

## 2.2. Gravity data

The later gravity data were collected using the LaCoste and Romberg (L&R) S129 gravity meter during the DY115-20 and DY115-21 cruises, the L&R S162 gravity meter during the DY125-30, DY125-34, and DY125-39 cruises, and the Dynamic Gravity Systems (DgS) advanced technology marine gravity meter during the DY125-40 cruise. We

performed the linear drift and Eötvös corrections to obtain gravity free-air anomalies (FAAs; Fig. S2b). The total length of the processed survey lines is  $>3.5 \times 10^4$  km, with a total of  $>6600$  crossovers (Fig. 2b). The root-mean-square of crossover errors of FAA is 3.4 mGal for the whole dataset (Fig. S2a), which is gridded with an interval of 0.5°.

We calculated the MBA map (Fig. 2c) by subtracting the predicted gravity effects of the water layer above the seafloor and a constant crustal thickness of 6 km from the FAA (Kuo and Forsyth, 1988), using GMT software gravity calculation ‘gravfft’ model (Wessel et al., 2019). The water, crust, and mantle densities were assumed to equal 1.03, 2.7, and  $3.3 \text{ g/cm}^3$ , respectively. Here, we ignored the gravity effect of a sedimentary layer because its thickness within the study area is not significant (Straume et al., 2019). To fully cover the area of enhanced magmatism, satellite bathymetry and gravity data (Sandwell and Smith, 2009; Weatherall et al., 2015) are used to fill the gap in shipboard data and generate a larger map of MBA with the approach mentioned above (Fig. 1b).

The residual MBA (RMBA; Fig. S2d) was calculated by removing the thermal correction that is the gravity effect of lithosphere cooling

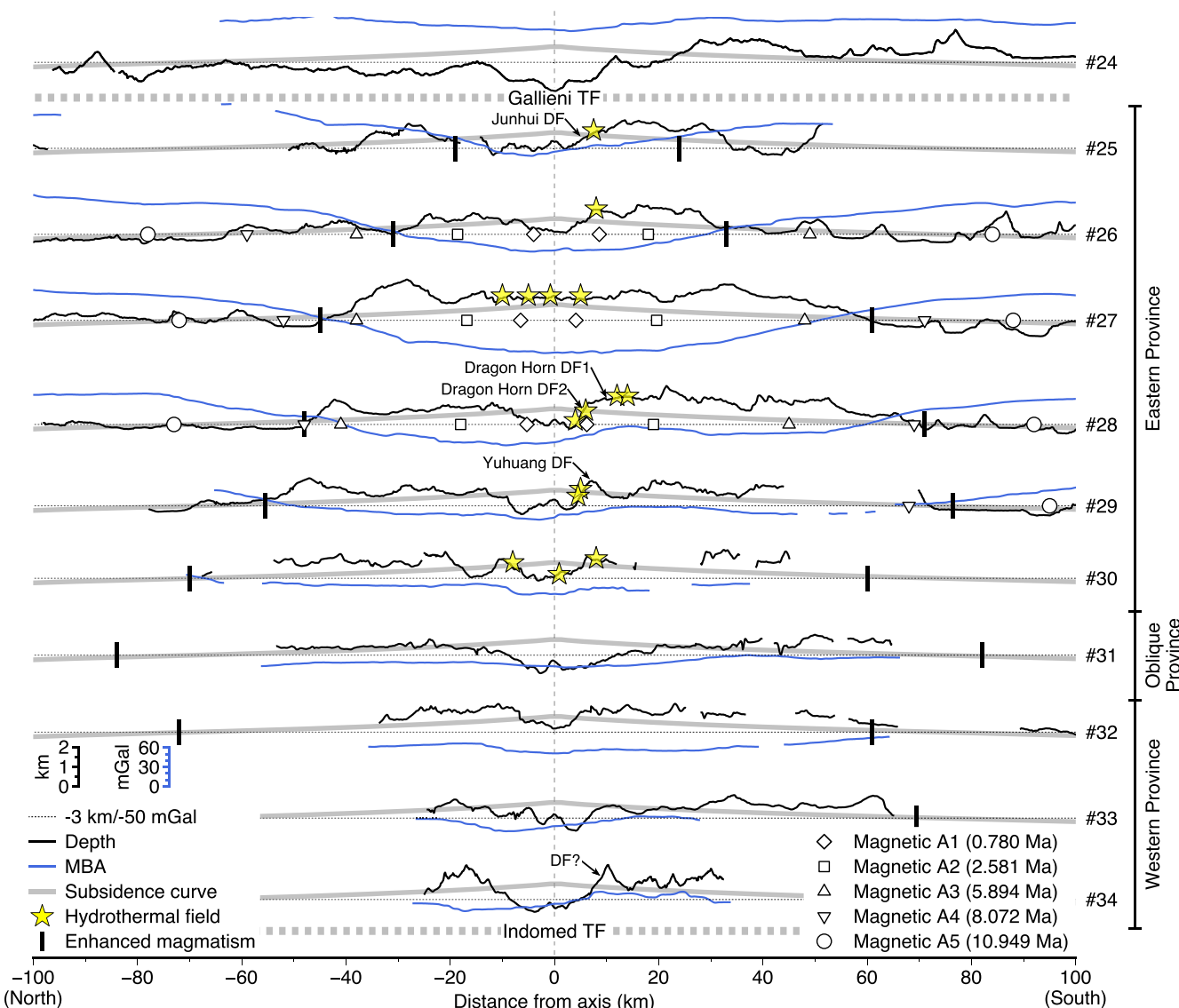


**Fig. 3.** Cross-axis sections of segments #24–#34. Profile locations are in Fig. 2a and c. Black and blue lines denote depth and MBA, respectively. Dotted horizontal lines mark the baselines of depth (-3 km) and MBA (-50 mGal). Thick gray lines are subsidence curves, predicted using the law of the square root of spreading age ( $T$ ) and the empirical depth ( $D$ ) by Parsons and Sclater (1977):  $D(T) = 340 T^{0.5} + D(T=0)$ , where assumes a symmetrical spreading around the location of the present-day ( $T=0$ ) ridge axis. (For interpretation of the references to colour in this figure legend, the reader is referred to the web version of this article.)

associated with spreading age. The mantle temperature field was calculated from spreading age at a constant half spreading rate of 7 km/Ma, then converted into mantle density variations (Kuo and Forsyth, 1988). We removed the gravity effect of these density variations (Fig. S2c) from MBA to obtain RMBA. To avoid edge effects at the ridge axis, our temperature field was cut by 25 km off-axis. RMBA is assumed only due to variations of crustal thickness that can be predicted by the downward continuation of the RMBA (Kuo and Forsyth, 1988). A filter with a cut-off wavelength between 20 and 30 km was applied to reduce short-wavelength anomalies. The crustal thickness at the center of segment #27 (50.5°E) is calibrated to the depth (9.5 km) of the seismic Moho interface (Jian et al., 2017; Li et al., 2015), yielding a crustal thickness map (Fig. 2d). A larger map of crustal thickness is also

generated with satellite gravity data filling the gap of shipboard data (Fig. S3).

### 3. Results

#### 3.1. Ridge segmentation

The SWIR between 46°E and 53.5°E includes two first-order segments bounded by the Indomed, Gallieni, and Gazelle TFs. The axial valley (~670 km along the ridge axis), bounded by the first pair of major inward-facing faults, has an average width of 18 km (Fig. 1a). It is cut off by a large swollen volcanic plateau around 50.5°E and offset ~110 km by the Gallieni TF. The first-order Indomed-Gallieni supersegment (580

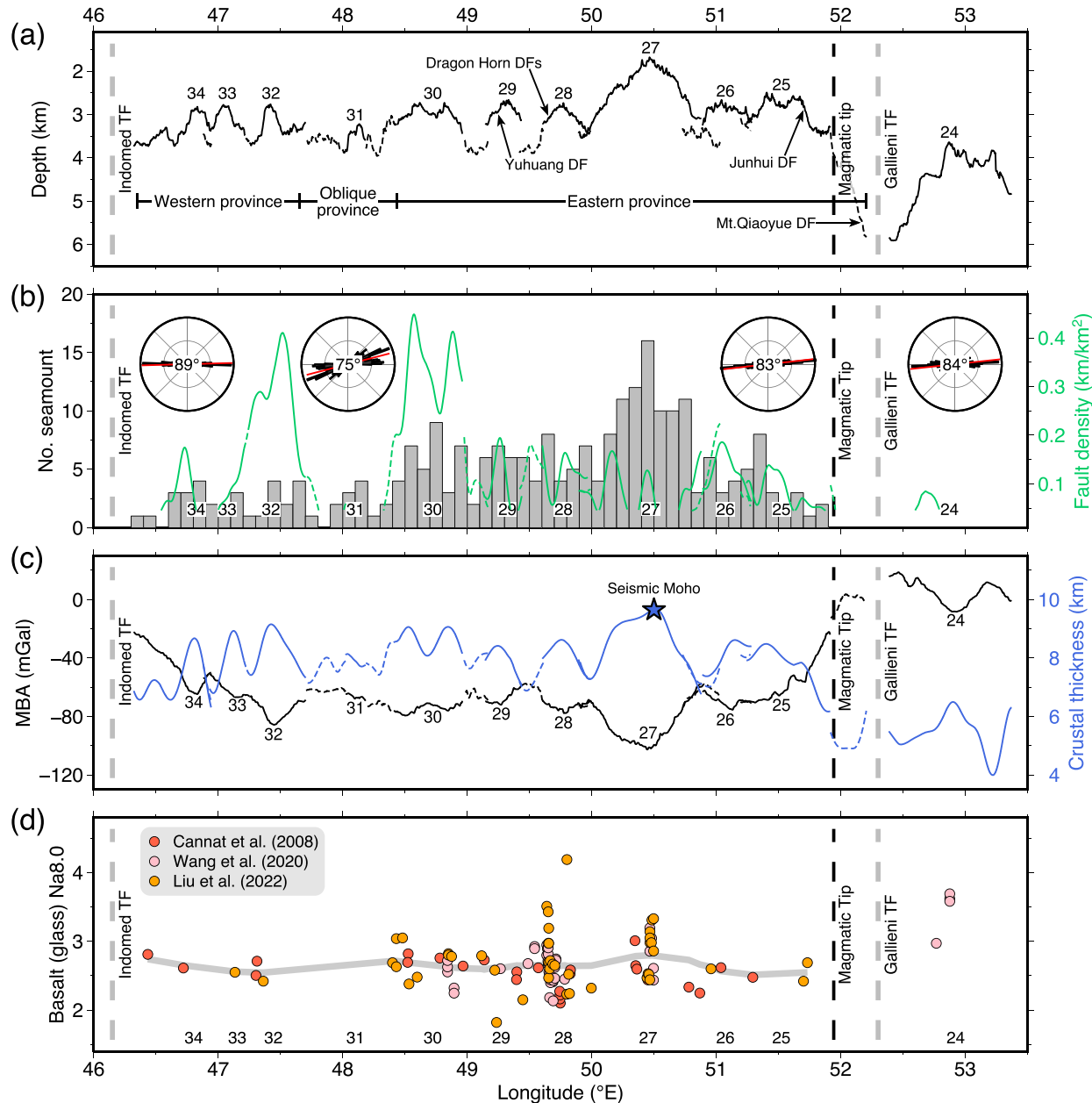


**Fig. 4.** Along-axis variations. (a) Depth profile. Locations of detachment faults (DFs) are labeled. (b) Seamount frequency and fault density. Seamounts are counted within 10 km off the axis (20 km in width) and binned by 0.1° in longitude. Rose maps from left to right represent the faults azimuths (black lines) and the average azimuths (red lines with values) of the Western, Oblique, and Eastern provinces as well as the Gallieni-Gazelle segment. (c) MBA and crustal thickness profiles. Crustal thickness at 50.5°E (the center of segment #27) is calibrated to the seismic Moho at 9.5 km (Jian et al., 2017; Li et al., 2015). (d) Na8.0 contents of basaltic glasses (Cannat et al., 2008; Liu et al., 2022; Wang et al., 2020). Thick gray line illustrates the long-wavelength variation of the Na8.0 contents. (For interpretation of the references to colour in this figure legend, the reader is referred to the web version of this article.)

km) can be divided into three provinces with dramatic changes in the ridge strike at longitudes of 47.67°E and 48.45°E (Fig. 1a). The general ridge strike in the Indomed-Gallieni supersegment is N72°. The ridge strike between the Indomed TF and 47.67°E is nearly east-west (N85°), changing to N47° between 47.67°E and 48.45°E and back to N75° between 48.45°E and the Gallieni TF. We, therefore, defined these three regions with distinct ridge strikes as the Western (125 km long), Oblique (100 km long), and Eastern (355 km long) provinces (Fig. 1a). The other first-order Gallieni-Gazelle segment is nearly east-west (93 km long). The average azimuths of faults follow the ridge strike, N89° for the Western province, N75° for the Oblique province, N83° for the Eastern province, and N84° for the Gallieni-Gazelle segment (Fig. 4b).

Ten second-order segments subdividing from the Western, Oblique, and Eastern provinces, and one single segment in the Gallieni-Gazelle segment, are numbered as segments #24–#34 from east to west

(Fig. 1), following the previous ridge segmentation study (Cannat et al., 1999a). Nontransform discontinuities (NTDs) that offset segments are numbered N25–N34 (Fig. 5). Segment length, measured between the deepest points of the adjacent NTDs, ranges between 15 and 93 km, and segments #24 (93 km), #25 (90 km), and #27 (85 km) are the longest ones (Table S1).

Using the bathymetry map (Figs. 1a and 5), we draw the ridge axis that should be the most recent volcanic activity and/or the center of tectonic deformation. It was picked along the crest of axial volcanic ridges (AVRs), centers of intra-rift volcanic ridges, or the deepest point within the NTDs. The ridge axes of segments #26–#28 have been well defined using bathymetry, gravity, and magnetic data (Cannat et al., 1999b; Sauter et al., 2001), and the ridge axis at the center of segment #27 (SWIR 50.5°E) was identified along the most recent eruptions using the AUV-based microbathymetry and magnetic data (Chen et al., 2021).

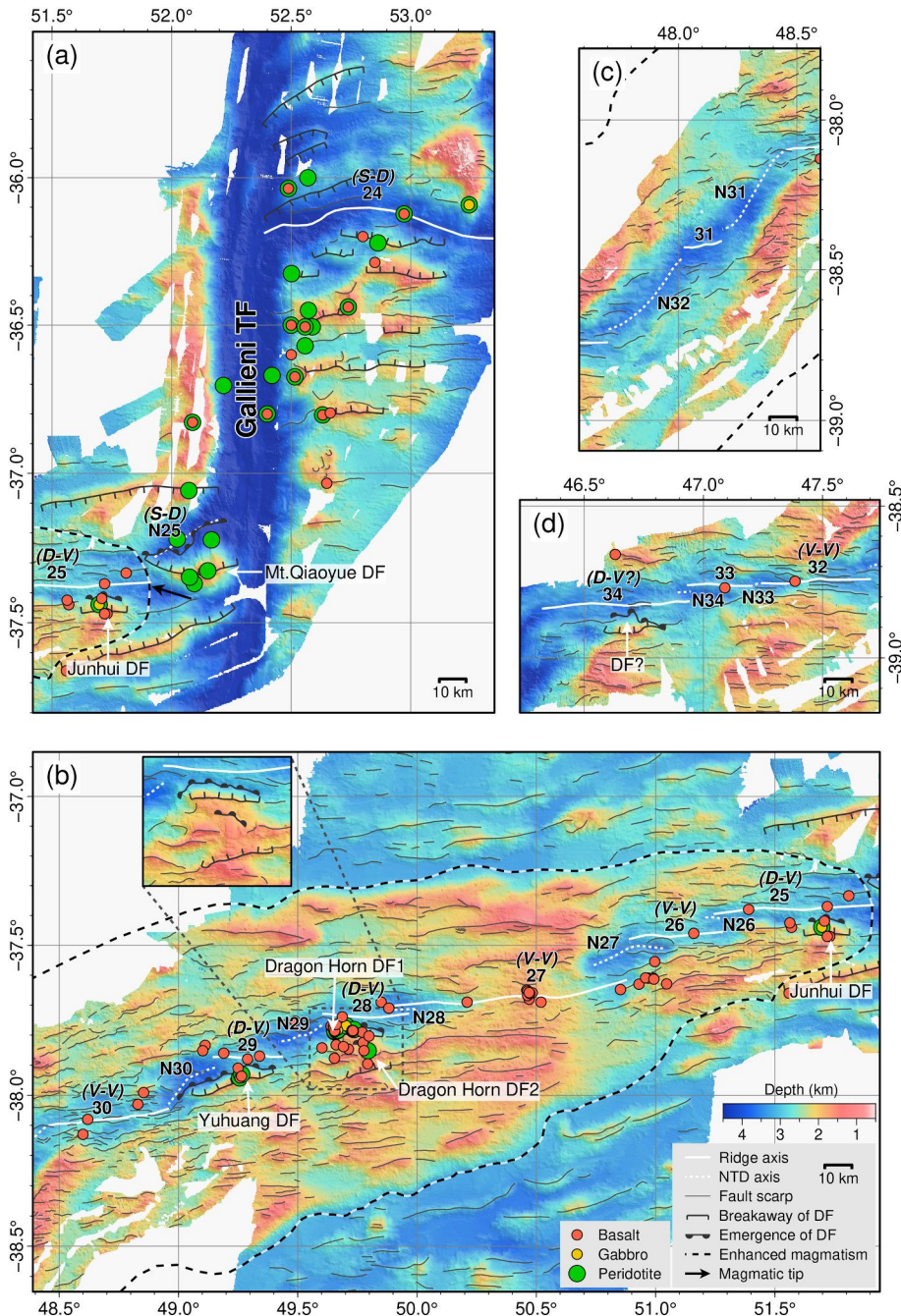


**Fig. 5.** Detailed bathymetry maps showing seafloor morphology and geological information. All figures have the same scales of distance and colour. See the legend for symbols in Fig. 5b. Locations and contents of rock samples are from multiple sources (Cannat et al., 2008; Huang et al., 2021; Liu et al., 2022; Yang et al., 2017; Yu and Dick, 2020; Zhou et al., 2022; Zhou and Dick, 2013). V-V: volcanic-volcanic mode. D-V: detachment-volcanic mode. S-D: successive detachment mode. (a) segment #25 and the region to the east of the magmatic tip. (b) Eastern province (segments #25–#30). The inset shows the close-up of the Dragon Horn DFs. (c) Oblique province (segment #31 and NTDs N31 and N32). (d) Western province (segments #32–#34).

A typical second-order segment is characterized by a topographic high and an MBA low at the segment center, and the topography deepens and the MBA increases gradually toward segment ends (Fig. 4). We do not classify two long-offset (up to 45 km), highly oblique ( $\sim N45^\circ$ ) NTDs N30 and N31 as second-order segments (Liu et al., 2020), because they do not have such topographic or gravity features along the axis (Figs. 4a and 5c).

### 3.2. Regional-scale enhanced magmatism

Our bathymetry and gravity maps outline a melt-rich domain characterized by abruptly elevated seafloor and significantly reduced MBAs between  $46.5^\circ\text{E}$  and  $51.9^\circ\text{E}$  (Figs. 1 and 2). The boundary of this melt-rich domain is partly identified based on the previous study (Sauter et al., 2009), in which bathymetry and gravity data only covered the off-axis seafloor between segments #26 and #28. The elevated seafloor and reduced MBAs synchronously show a V shape in the Eastern province, narrowing from segment #30 ( $\sim 130$  km wide) to a magmatic tip ( $51.9^\circ\text{E}$ ) that is  $\sim 30$  km to the west of the Gallieni TF (Figs. 1 and 5a). Due to the inadequate off-axis data in the Western and Oblique provinces, the boundary of the melt-rich domain is drawn by a combination of shipboard and satellite-derived data (Fig. 1). There, the width of the melt-rich domain is almost constant at  $\sim 140$  km, with no evidence of a V shape.

Along-axis depth and MBA profiles in Fig. 4 show contrasting features to the west ( $46\text{--}51.9^\circ\text{E}$ ) and to the east ( $51.9\text{--}53.5^\circ\text{E}$ ) of the tip; the mean depth and the mean MBA to the west of the tip are 3150 m and -67 mGal, 1300 m shallower and 70 mGal lower than those to the east, respectively. Numerous volcanic seamounts and frequent faults (high fault density) are observed inside the melt-rich domain, while outside this domain, seamounts are nearly absent, and faults are widely spaced with a lower fault density (Figs. 2a, 4b, and S1c). The average crustal thickness inside the melt-rich domain is  $\sim 7.5$  km, which is 1.5 and 3 km thicker than the region outside the melt-rich domain of the flanks at

segments #26–#28 and the region to the east of the magmatic tip, respectively (Fig. 2d).

### 3.3. Segment-scale variations of melt supply

Inside the melt-rich domain, segment #27 is the most magmatically-robust segment, and its segment center at  $50.5^\circ\text{E}$  is the present magmatic apex. This segment is characterized by highly elevated seafloor (shallows to  $\sim 1650$  m at the segment center), a higher density of volcanic seamounts, conjugate faults rifting domal volcanoes and extending up to 65 km along the axis, the lowest MBA (down to -100 mGal) with a well-defined circular MBA low, i.e., the ‘bull eyes’ pattern (Figs. 2 and 5b) (Lin et al., 1990), and the thickest crust (9.5 km) (Li et al., 2015). Segment #32 has the second magmatically-robust feature, also corresponding to a circular MBA low (down to -85 mGal) and a crustal thickness of up to 9 km. AVR s are observed at segments #25, #26, #28, #29, #31, #33, and #34, with relatively small MBA lows and thinner crusts (Figs. 4c and 5), indicating moderate magmatism. Segments #30 and #32 are highly fractured, with frequent faults on both flanks with no well-defined AVR s (Fig. 5b and d). The spacing of discrete magmatic centers in the Indomed-Gallieni supersegment, i.e., the spacing of spreading cells (Carbotte et al., 2015), is 30–70 km with an average of 55 km. In cross-sections, the seafloor inside the melt-rich domain does not follow the subsidence curves, especially at segments #27–#29 (Fig. 3).

Detachment faults (DFs) and oceanic core complexes (OCCs) with exposure of gabbros and peridotites are observed at south flanks of segments #25 (Junhui DF), #28 (Dragon Horn DF1 and Dragon Horn DF2), and #29 (Yuhuang DF), corresponding to more elevated seafloor, more positive MBAs, and thinner crusts, relative to their conjugate flanks (Figs. 3, 5, and 6). According to this criterion, we suspect a detachment fault to be located at the south flank of segment #34, despite no sampling evidence yet (Figs. 3 and 5d). We also found that the inside corner of the Oblique province (i.e., the southern plate of

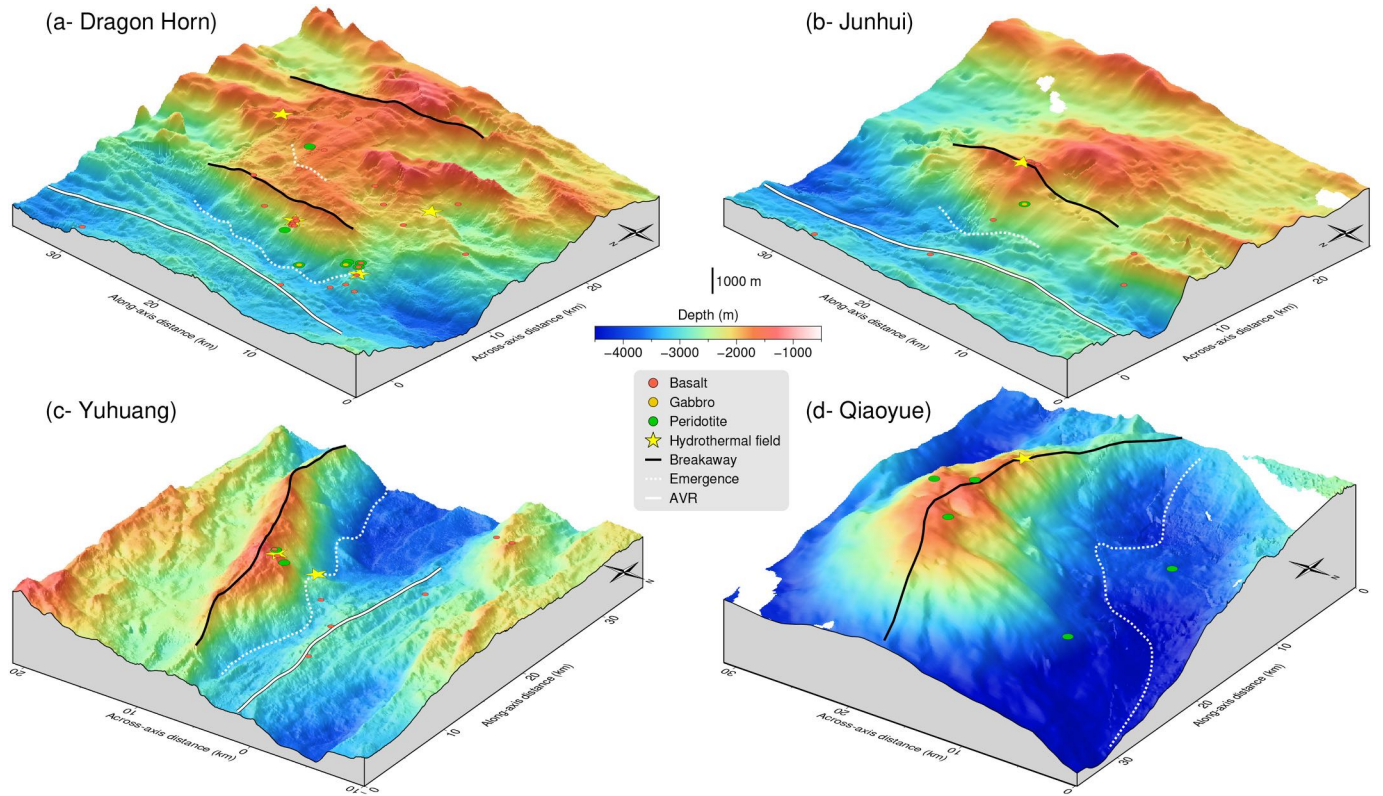


**Fig. 6.** 3-D views showing Dragon Horn (a), Junhui (b), Yuhuang (c), and Qiaoyue (d) detachment faults with the same distance scale. See locations in Fig. 5.

segments #28-30) has ~0.8 km thinner crust than the outside corner in the conjugate plate (Fig. 2d).

Outside the melt-rich domain, we differentiate three areas: the deepest part at flanks of segments #26-#28, the ridge section between the magmatic tip and the Gallieni TF, and segment #24 to the east of the Gallieni TF (Fig. 5a and b). All three areas are characterized by the absence of volcanic morphological features (e.g., no seamounts) and a deep basement capped by widely spaced axis-parallel ridges with no corrugations (Fig. 5a and b). In the deepest part at flanks of segments #26-#28 (Fig. 5b), the seafloor is relatively flat (probably due to a sediment layer) with faults that are up to 50 km long and 1500 m relief, and this area follows well with the subsidence curves (Fig. 3). Between the magmatic tip and the Gallieni TF, the seafloor deepens 2000 m, and MBA increases ~25 mGal from west to east. The near-axis Mt. Qiaoyue DF is ~30 km long with a high relief of 3500 m, and two off-axis ridges are ~60 km long with lower reliefs of 1500 m; these three ridges have a smooth, rounded topography (Figs. 5a and 6d). At segment #24, a topographic high and an MBA low are observed at the segment center with very few volcanic features (Figs. 4 and 5a). Off-axis ridges (10-60

km long) with a smooth, rounded topography are almost evenly distributed on the south and north flanks (Fig. 5a).

#### 4. Discussion

##### 4.1. Comparison of gravity-derived and seismic crustal thicknesses

We compare gravity-derived and seismic crustal thicknesses around the center of segment #27 (Fig. 7), where a 3-D seismic experiment has been carried out within a  $40 \times 40 \text{ km}^2$  box (Jian et al., 2017; Li et al., 2015). The gravity-derived crustal thickness at the center of segment #27 ( $50.5^\circ\text{E}$ ) is calibrated to 9.5 km by seismic data (Jian et al., 2017; Li et al., 2015). The along-axis misfits of crustal thickness increase from the segment center toward segment ends, while across-axis misfits are minor (Fig. 7d and e). We link the along-axis misfits with mean crustal density variations that are mainly contributed by gabbroic layer 3 (Tolstoy et al., 1993). The segment center corresponds to the thickest gabbroic layer 3 (up to 6.7 km) and hence the lowest mean crustal density, whereas segment ends (20 km toward the segment center) correspond to a

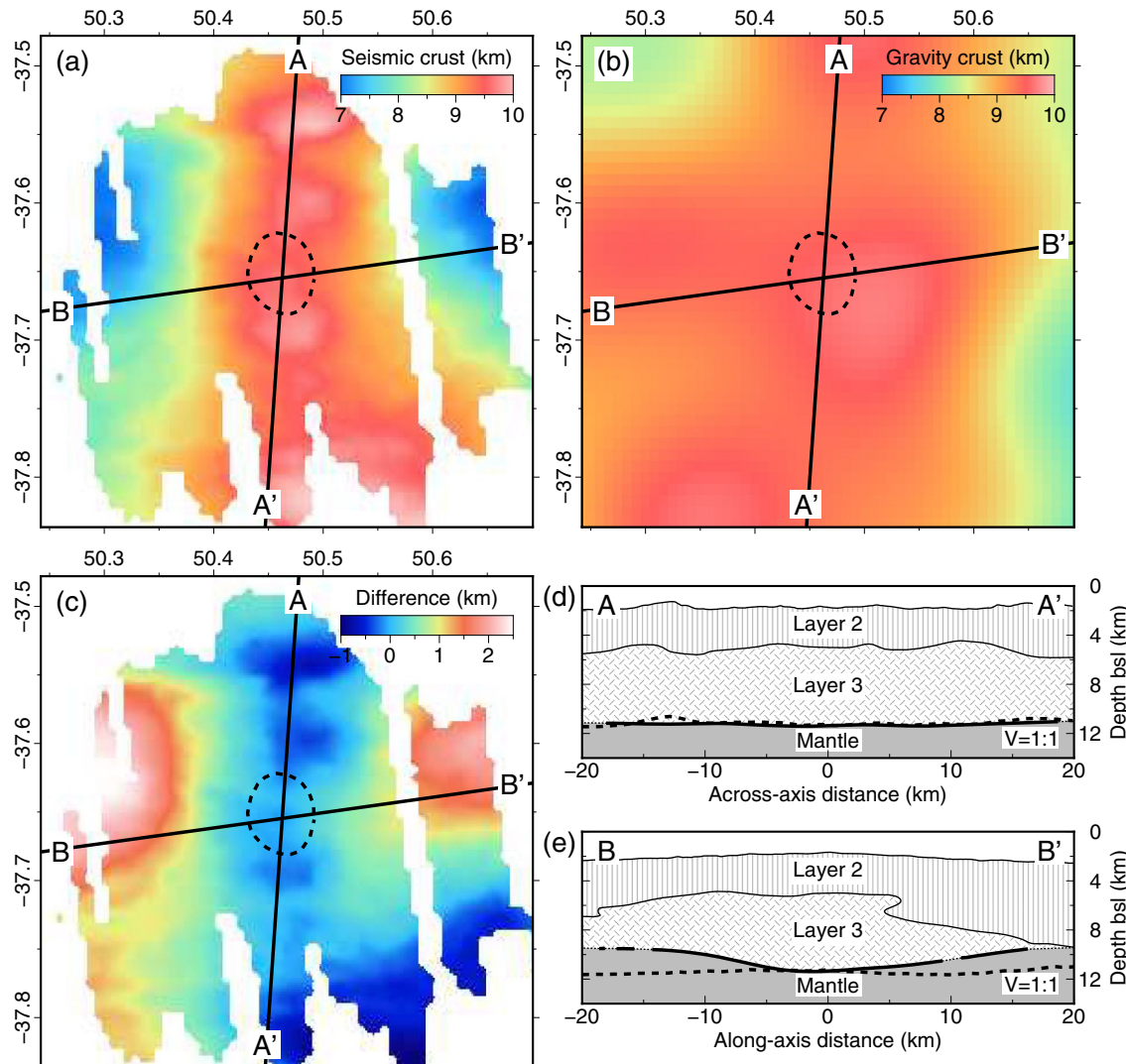


**Fig. 7.** Comparison of gravity-derived and seismic crustal thicknesses at the center of segment #27. (a) Seismic crustal thickness, defined as depths to the Moho interfaces (Jian et al., 2017; Li et al., 2015). Dashed lines outline the seismic low-velocity anomaly of  $-0.4 \text{ km/s}$  at 7 km below the seafloor (Jian et al., 2017; Li et al., 2015). Profiles AA' and BB' are shown in (d) and (e). (b) Gravity-derived crustal thickness (see the location in Fig. 2d), calibrated to 9.5 km at the center of segment #27 by seismic data (Jian et al., 2017; Li et al., 2015). (c) Difference of crustal thickness between seismic and gravity data. (d) and (e) Across- and along-axis crustal structure. The boundary of crustal layers 2 and 3 is defined by a velocity gradient contour at  $0.3 \text{ s}^{-1}$  (Jian et al., 2017; Li et al., 2015). Thick solid and dashed lines represent the seismic and gravity-derived Moho interface, respectively.

thinner or even disappeared layer 3 and hence higher mean density. The seismic low-velocity anomaly at the segment center, interpreted as a hot low-crustal mush zone (Jian et al., 2017; Li et al., 2015), could further lower the mean crustal density at the segment center. Our gravity model ideally applied the assumption of a homogeneous crustal density, resulting in the crustal thickness underestimated at segment centers and/or overestimated at segment ends and displaying a smoother crustal variation than seismic data. This discrepancy between the seismic and gravity-derived crustal thickness has also been discussed for the MAR (Tolstoy et al., 1993). We take this into account in our interpretations and discussion.

#### 4.2. Spatial and temporal evolution of enhanced magmatism and its origin

We divided the study area into stripes separated by isochrons (axis A1, A1-A2, A2-A3, A3-A4, and A4-A5; Fig. S3) to obtain along-axis, time-average crustal thickness resulting from the enhanced magmatism. These isochrons are mainly constrained by magnetic anomaly picks (Sauter et al., 2009), as well as by spreading distance from the ridge axis (assuming a constant half spreading rate of 7 km/Ma) and a global dataset of crustal age (Seton et al., 2020) for areas without magnetic

picks. The magnetic anomalies from A1 to A5 correspond to 0.78, 2.581, 5.894, 8.072, and 10.949 Ma, respectively (Sauter et al., 2009); we mainly use magnetic anomalies A1-A5 in the following for the convenience of discussion. We subtract a referenced crustal thickness from the along-axis, time-average crustal thickness of each stripe to get crustal thickness anomalies in Fig. 8a. For this referenced crustal thickness, we take the mean thickness value of 6 km in the area beyond A5 between 49° and 51.5°E (covered by shipboard gravity and bathymetric data), inferred to be unaffected by the enhanced magmatism (Fig. S3).

Positive anomalies of crustal thickness initially occurred between A5 and A4 in the Western and Oblique provinces, as well as segment #30 of the Eastern provinces (Fig. 8a). There is no evidence for a magmatic propagation in the Western and Oblique provinces, and segment #32 has received the highest melt supply since A4. In the Eastern province, positive anomalies of crustal thickness eastwardly propagated from segment #30 to the magmatic tip between A5-A4 and A1, and segment #27 has received the highest melt supply since A3 (Fig. 8a). This eastward propagation has a mean velocity of ~30 km/Ma between segments #28 and #26 at 8.1-4.2 Ma ago (Sauter et al., 2009), and of ~20 km/Ma between segment #25 and the magmatic tip at 4.2-0.78 Ma ago.

Fig. 8b shows the time-average crustal volume anomalies per unit

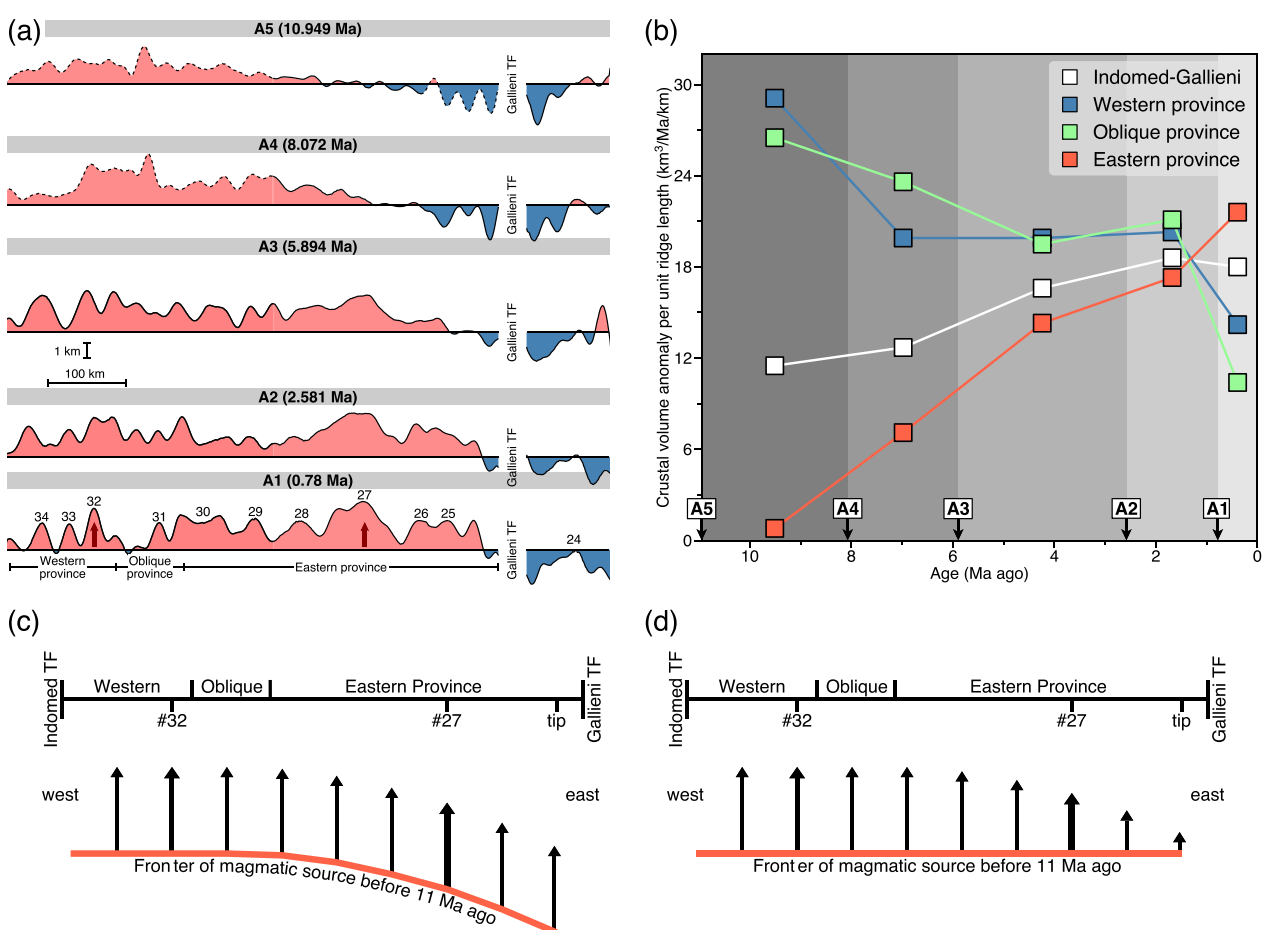


**Fig. 8.** Spatial and temporal evolution of the enhanced magmatism of the Indomed-Gallieni supersegment. (a) Along-axis, time-averaged crustal thickness anomalies of the melt-rich domain, calculated by subtracting the referenced mean crustal thickness (6 km) in the area beyond A5 and between 49° and 51.5°E with shipboard gravity and bathymetry data (vertical stripes in Fig. S3), which is not affected by the enhanced magmatism. Positive (red) and negative (blue) anomalies are filled. Solid and dashed outlines indicate that crustal thicknesses are derived from the hipboard and satellite data, respectively. (b) Time-average crustal volume anomalies per unit ridge length along the whole Indomed-Gallieni supersegment (white squares) as well as the Western (blue squares), Oblique (green squares), and Eastern (red squares) provinces. (c) and (d) Possible geometry of the frontier (i.e., the depth where the anomalous melting began) of anomalous magmatic source before 11 Ma ago. In the Western and Oblique provinces, the frontier of the magmatic source is probably horizontal with a homogenous upwelling rate. In the Eastern province, (c) if the upwelling rate of the magmatic source is the same as that of the Western and Oblique provinces, its frontier may have a slope facing east, (d) and if the frontier is horizontal, the upwelling rate may decrease from west to east. Thicker arrows represent two magmatic centers at segments #27 and #32. (For interpretation of the references to colour in this figure legend, the reader is referred to the web version of this article.)

ridge length along the whole Indomed-Gallieni supersegment and three provinces. The crustal anomaly in the whole Indomed-Gallieni supersegment increased from 11.5 to  $\sim 18$  km<sup>3</sup>/Ma/km between A5 and the present. Since A5, the Western and Oblique provinces have received decreased melt volumes from 29.1 and 26.5 to 14.2 and 10.4 km<sup>3</sup>/Ma/km, respectively, while the Eastern province has received increased melt volumes from 0.8 to 21.6 km<sup>3</sup>/Ma/km (Fig. 8b).

The origin of the enhanced magmatism at the Indomed-Gallieni supersegment is still being discussed. Some authors hypothesized it as the interaction between the SWIR and the Crozet hotspot that is 800–1000 km to the south of the SWIR (Breton et al., 2013; Sauter et al., 2009; Yang et al., 2017; Zhang et al., 2013), which may cause anomalous mantle temperatures and/or compositions beneath the Indomed-Gallieni supersegment. Although our shipboard dataset cannot verify this ridge-hotspot interaction due to the spatial limitation, our results show that the excess crustal production at the peak of the enhanced magmatism between A2 and A1 ( $\sim 1 \times 10^4$  km<sup>3</sup>/Ma) is one order of magnitude smaller than the Galapagos Spreading Center influenced by the off-axis (200 km) Galapagos hotspot or the Reykjanes Ridge influenced by the on-axis Iceland hotspot ( $3 \pm 2 \times 10^5$  km<sup>3</sup>/Ma) (Sallarès and Charvis, 2003).

Alternatively, the enhanced magmatism may be attributed to the enrichment of water in the mantle (Liu et al., 2022), which could result in a greater depth of the initiation of mantle melting and thus more melt productions (Asimow and Langmuir, 2003). This water involvement in mantle melting is interpreted as recycled from an ancient wedge mantle residual (Liu et al., 2022; Wang et al., 2020; Yu and Dick, 2020). The impact of the water involvement may be limited within the Indomed-Gallieni supersegment (Liu et al., 2022), as its adjacent ridge sections have an overall low melt supply with widespread peridotites (Zhou and Dick, 2013).

No matter what the origin of the enhanced magmatism is (e.g., anomalous temperatures, compositions, and/or dynamics of the mantle melting), it increased crustal productions, started in the Western and Oblique provinces at almost the same time, and later occurred in the Eastern province with a decreased velocity of eastward propagation. The geometry of the anomalous magmatic source with buoyant mantle upwelling may be responsible for the change of the enhanced magmatism, e.g., the Reykjanes Ridge (Martinez and Hey, 2017) and the Azores Platform in the northern MAR (Cannat et al., 1999b). Thus, we interpret that before 11 Ma ago, the magmatic source in the Western and Oblique provinces may have a horizontal frontier (i.e., the depth where the anomalous melting began) and upwell at a relatively homogenous rate (Fig. 8c and d), which should be overall shallower and/or have a faster upwelling rate than the later interaction at the Eastern province. In this later interaction, if the upwelling rate of the magmatic source is homogenous before 11 Ma ago, its frontier may have a slope facing east (Fig. 8c), and if the frontier is horizontal, the upwelling rate may decrease from west to east (Fig. 8d). Both hypotheses can form a plane-view, V-shaped propagation with a decreased velocity. The two (western and eastern) magmatic centers at segments #32 and #27 may be derived from locally extreme melt focusing (Li et al., 2015) and/or the heterogeneity of the magmatic source.

#### 4.3. The impact of the enhanced magmatism

##### 4.3.1. Ridge geometry

The ridge geometry at ultraslow spreading ridges is commonly controlled by the combination of orthogonal volcanic and oblique nonvolcanic regions (Dick et al., 2003; Sauter et al., 2001), like what has been observed in our study area. This orthogonal-oblique ridge geometry may be stable for millions of years or modified by changes of spreading rate and/or melt supply (Cannat et al., 2008; Dick et al., 2003). Satellite-derived bathymetry outside the melt-rich domain of the Oblique province shows that spreading-parallel fracture zones were cut off by the elevated domain (Fig. 1a). In addition, three more oblique

sections at the south edge of the enhanced magmatism at longitudes of 49.55°E, 50.55°E, and 51.1°E (Fig. 5b) indicate ridge jumps, presumably associated with the discontinuity of the eastward magmatic propagation (Sauter et al., 2009). Therefore, we propose that the plate boundary between the Indomed and Gallieni TFSs may have been reorganized 11–8 Ma ago due to the melting event, as the spreading rate did not change. More intensive geophysical survey lines are needed to better understand these changes in ridge geometry and their connections to magmatism.

##### 4.3.2. Attenuation of melt focusing

To describe the melt focusing on the segment scale, we compare along-axis MBA amplitude ( $\Delta$ MBA) versus segment length (L) in Fig. 9. Positive correlations of L and  $\Delta$ MBA (i.e., a longer segment generally has a greater  $\Delta$ MBA) have been documented at the melt-poor easternmost SWIR (Cannat et al., 1999a) and the slow spreading MAR 15–38°N (Detrick et al., 1995; Lin et al., 1990; Thibaud et al., 1998), and at a given segment length, a higher  $\Delta$ MBA at the melt-poor easternmost SWIR suggests a higher degree of melt focusing, corresponding to a larger axial variation of crustal thickness and/or mantle temperature (Cannat et al., 1999b). In the Indomed-Gallieni supersegment, there is also a positive correlation between segment length and  $\Delta$ MBA, as we consider  $\Delta$ MBAs of segments #32 and #33 as a single segment because the offset at their intervening NTD is not significant ( $\sim 3$  km) and the MBA variation in between is weak (Fig. 4c). The fitting line of the Indomed-Gallieni supersegment is almost the same as the MAR 15–38°N but below the melt-poor easternmost SWIR (Fig. 9 and a similar pattern for along-axis relief versus segment length in Fig. S4), suggesting that the degree of melt focusing (i.e., crustal thickness variation) at the Indomed-Gallieni supersegment is close to the MAR 15–38°N but lower than the melt-poor easternmost SWIR.

Comparing seismically documented segments of the Indomed-Gallieni supersegment and the MAR 15–38°N, segment #28 and segment 34°N (OH-3) of the MAR have similar lengths of 40–45 km, corresponding to similar crustal thickness variations of 3–3.3 km and 2.4–3.9 km, respectively (Hooft et al., 2000; Li et al., 2015; Zhao et al., 2013). As for longer segments, segment #27 and segments 35°N (OH-1) and 21.5°N of the MAR also have similar lengths of 85–90 km, corresponding to crustal thickness variations of 5.5 km, 3.5–4.5 km, and 2.5–4 km, respectively (Dannowski et al., 2011; Hooft et al., 2000; Li et al.,

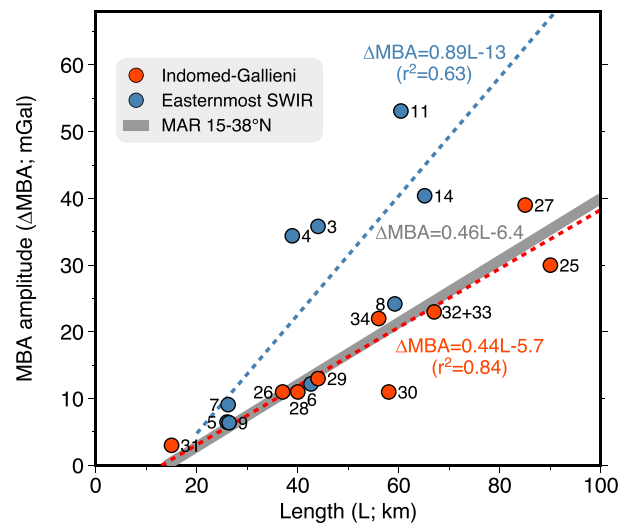


**Fig. 9.** Along-axis MBA amplitude ( $\Delta$ MBA) as a function of segment length (L). Data included are the Indomed-Gallieni (red circles and red dashed fitting line by this study), the easternmost SWIR (blue circles and blue dashed fitting line) (Cannat et al., 1999a), and the slow spreading MAR 15–38°N (thick gray fitting line) (Detrick et al., 1995; Lin et al., 1990; Thibaud et al., 1998). (For interpretation of the references to colour in this figure legend, the reader is referred to the web version of this article.)

2015). It is not surprising to have a higher variation at segment #27 as its  $\Delta$ MBA has a positive deviation from the fitting line (Fig. 9), which is interpreted as a local high degree of melt focusing (Li et al., 2015).

We also compared along-axis basalt (glass) Na8.0 contents between 46°E and 53.5°E (Cannat et al., 2008; Liu et al., 2022; Wang et al., 2020), which reveals a nearly uniform pattern inside the melt-rich domain (including the most magmatically-robust segment #27) and thus suggests very small variations in the degree of melting (Fig. 4). We, therefore, propose that segment-scale melt focusing at the Indomed-Gallieni supersegment is lowered by the enhanced magmatism with two possible explanations. First, since the cold lithosphere depresses the top of the melting region and since the thickening of the axial lithosphere at segment ends results in lower melt production than their corresponding segment centers (Bell and Buck, 1992; Magde et al., 1997; Sauter et al., 2001), the axial variation of lithosphere thickness may be decreased due to extra heat released by the buoyant magmatic source. This hypothesis is supported by microearthquakes recorded by ocean-bottom seismometers; the maximum depth of earthquakes determines a mostly homogenous axial lithosphere thickness along segment #28 (Yu et al., 2018). Although the degree of melt focusing in the study area is comparable to the slow spreading MAR, the lithosphere thickness at segment #28 is about twice thicker than the MAR 26° and 29°N (15 vs. 8–10 km) (de Martin et al., 2007; Wolfe et al., 1995; Yu et al., 2018), which probably results from shallower melt emplacement and thus more efficient hydrothermal heat extraction in our study area (Chen et al., 2022). Second, the melt may be redistributed in the lower crust that is hot enough to transport melt from segment centers to ends (Jian et al., 2017; Magde et al., 1997; Sauter et al., 2001).

#### 4.4. Melt supply, faulting pattern, and seafloor spreading modes

The pattern of faulting at slow and ultraslow spreading ridges is highly sensitive to melt supply, associated with diverse seafloor spreading modes (Cannat et al., 2019; Cannat et al., 2006; Escartín et al., 2008; Liu and Buck, 2020). For example, dramatic changes in melt supply over an along-axis distance of <30 km (away from any TFs) at the easternmost SWIR are correlated with spreading modes and faulting patterns changing from successive flip-flop detachment faults with nearly zero melt supply to frequent high-angle normal faults with moderate melt supply (Cannat et al., 2019).

The variability of melt supply at the SWIR 46–53.5°E is even larger than at the easternmost SWIR, which is bracketed by two endmembers,

the most magmatically-robust endmember at the center of segment #27 (50.5°E) and nearly zero melt supply to the east of the magmatic tip (51.9–53.5°E). At the center of segment #27, crustal thickness is up to 9.5 km (Jian et al., 2017; Li et al., 2015) with conjugate faults at lengths of up to 65 km (Fig. 5b). In addition, the measurement of apparent faults based on microbathymetry data suggests that the magmatic contribution to the plate spreading (M value) (Buck et al., 2005), is over 90%, i.e.,  $M > 0.9$  (Chen et al., 2021). In contrast, to the east of the magmatic tip, the seafloor is characterized by widely spaced, rounded, smooth ridges (Fig. 5a) with extensive peridotites on both ridge flanks (Huang et al., 2021; Zhou and Dick, 2013). This region is similar to the smooth seafloor around the nearly-amagmatic SWIR 64.5°E (close-up views in Fig. 10 for comparison), which is generated by successive flip-flop detachment faults that accommodate almost 100% of the plate spreading ( $M = \sim 0$ ) and continuously exhume mantle-derived peridotites onto the seafloor (Cannat et al., 2019; Cannat et al., 2006; Sauter et al., 2013). We, therefore, propose that the region to the east of the magmatic tip may similarly be controlled by successive flip-flop detachment faults. The near-axis Mt. Qiaoyue DF, between the magmatic tip and the Gallieni TF, should be the youngest detachment fault, and two off-axis ridges are older detachments (Fig. 5a).

The youngest Mt. Qiaoyue DF is only half the length of two older detachments, and these two older detachments also bracket the Junhui DF (detachment facing volcanic seafloor) and the center of segment #25 (volcanic facing volcanic seafloor with frequent high-angle normal faults; Fig. 5a). This suggests that over an along-axis distance of  $\sim 60$  km near the magmatic tip, the eastward propagation of the enhanced magmatism modifies the seafloor spreading from flip-flop detachment, detachment-volcanic, to volcanic-volcanic modes. In the study area, similar detachment-volcanic spreading modes can be observed at segments #28, #29, and possibly #34, and similar volcanic-volcanic spreading modes can be observed at segments #26, #30, and #32 (Figs. 3 and 5), which are also commonly observed at slow and ultraslow spreading ridges (Cannat et al., 2006; Escartín et al., 2008; Mendel et al., 2003; Zhou et al., 2022).

The SWIR 46–53.5°E, therefore, displays the full spectrum of melt supply, M value, and faulting patterns among ultraslow spreading ridges; these spectrums can be identified within a minimum along-axis distance of 160 km between the center of segment #27 (50.5°E) and the Gallieni TF. Recent numerical modeling predicted that faulting patterns and spreading modes coincide with changes of melt supply at an ultraslow spreading rate (Liu and Buck, 2020), which provides

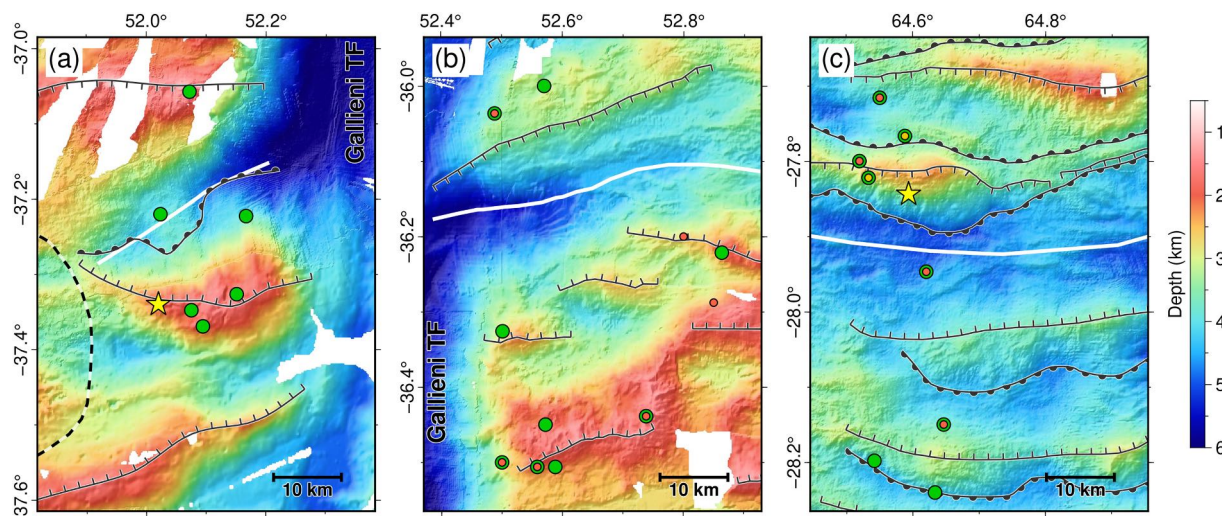


**Fig. 10.** Close-up views of bathymetry maps with the same distance and colour scales, showing seafloor morphology and faulting pattern of the nearly-amagmatic regions of the SWIR. Same legend as Fig. 5b. (a) The region between the magmatic tip and the Gallieni TF, (b) Segment #24 to the east of the Gallieni TF, (c) Smooth seafloor at the easternmost SWIR (Cannat et al., 2006; Sauter et al., 2013).

implications for the spreading process of the SWIR 46–53.5°E. As melt supply decreases from the most robust to nearly zero, seafloor spreading processes change from volcanic-volcanic mode with nearly no faults (the center of segment #27), volcanic-volcanic mode with frequent normal faults (segments #26, #30, and #32), detachment-volcanic mode (segments #25, #28, #29, and possibly #34), to successive detachments mode (the region to the east of the magmatic tip).

## 5. Conclusions

Based on the combination of shipboard bathymetry and gravity datasets, we identified 11 second-order segments (#24–#34) and mapped geological features (faults and volcanic seamounts) at the SWIR 46–53.5°E. We provided new insights into the spatial and temporal evolution of the enhanced magmatism in the Indomed-Gallieni supersegment. The enhanced magmatism initiated in the Western and Oblique provinces 11 Ma ago with no propagation and a decreasing melt supply, while in the Eastern province, there is an eastward magmatic propagation with an increasing melt supply and a decreasing propagating velocity. The present propagation tip is at 51.9°E, ~30 km to the west of the Gallieni TF. We further attribute the change of the enhanced magmatism to the interaction with an anomalous magmatic source, and differences of upwelling rates and/or geometry of this source may play important roles. The enhanced magmatism changed ridge segmentation of the Indomed-Gallieni supersegment by lowering the spacing of magmatic centers and the degree of segment-scale melt focusing, typical of what is observed at the slow spreading MAR. As magmatism dramatically decreases from the most robust (9.5 km-thick-crust at 50.5°E) to nearly zero (near the Gallieni TF) over an along-axis distance of 160 km, ultraslow seafloor spreading systematically changes from volcanic-volcanic mode with very few faults to successive flip-flop detachment mode.

## CRediT authorship contribution statement

**Jie Chen:** Conceptualization, Formal analysis, Methodology, Software, Visualization, Writing – original draft, Writing – review & editing. **Tao Zhang:** Conceptualization, Data curation, Funding acquisition, Investigation, Methodology, Supervision, Validation, Writing – review & editing. **Huaiming Li:** Conceptualization, Data curation, Funding acquisition, Investigation, Project administration, Supervision, Validation. **Chunhui Tao:** Funding acquisition, Investigation, Project administration, Supervision, Validation. **Mathilde Cannat:** Conceptualization, Methodology, Supervision, Validation, Writing – review & editing. **Daniel Sauter:** Conceptualization, Validation, Writing – review & editing.

## Declaration of Competing Interest

The authors declare that they have no known competing financial interests or personal relationships that could have appeared to influence the work reported in this paper.

## Data availability

We have shared data in Figshare: <https://doi.org/10.6084/m9.figshare.22689784>

## Acknowledgments

We are grateful to the captains and the crew of R/V Dayang Yihao and R/V Xiangyang Hong 10 for their efforts in data acquisition from 2008 to 2016. The data collected during the Gallieni and SWIFT cruises are publicly available (<https://www.seanoe.org/data/00794/90636/>; <https://www.seanoe.org/data/00483/59494/>). The data collected during the DY cruises are available on request from corresponding

authors. Grids of MBA, RMBA, and crustal thickness and locations of ridge axis, faults, and seamounts are stored in Figshare (<https://doi.org/10.6084/m9.figshare.22689784>). We thank Deborah Smith and an anonymous reviewer for their insightful comments. Figures are generated using GMT 6. Tao Zhang and Chunhui Tao were supported by the Natural Science Foundation of China (41976079 and 42127807, respectively). Data acquisition and processing during DY cruises were supported by the China Ocean Mineral R&D Association Project (DY135-S1-01) and the National Key Research and Development Program of China (2018YFC0309901). Jie Chen was partly supported by China Scholarship Council (201808330437). This is IPGP contribution #4246.

## Appendix A. Supplementary data

Supplementary data to this article can be found online at <https://doi.org/10.1016/j.tecto.2023.229903>.

## References

- Asimow, P.D., Langmuir, C.H., 2003. The importance of water to oceanic mantle melting regimes. *Nature* 421, 815–820. <https://doi.org/10.1038/nature01429>.
- Bell, R.E., Buck, W.R., 1992. Crustal control of ridge segmentation inferred from observations of the Reykjanes ridge. *Nature* 357. <https://doi.org/10.1038/357583a0>.
- Breton, T., Nauvert, F., Pichat, S., Moine, B., Moreira, M., Rose-Koga, E.F., Auclair, D., Bosq, C., Wavrunt, L.M., 2013. Geochemical heterogeneities within the Crozet hotspot. *Earth Planet. Sci. Lett.* 376, 126–136. <https://doi.org/10.1016/j.epsl.2013.06.020>.
- Buck, W.R., Lavier, L.L., Poliakov, A.N.B., 2005. Modes of faulting at mid-ocean ridges. *Nature* 434, 719–723. <https://doi.org/10.1038/nature03358>.
- Cannat, M., Rommevaux-Jestin, C., Sauter, D., Deplus, C., Mendel, V., 1999a. Formation of the axial relief at the very slow spreading Southwest Indian Ridge (49° to 69°E). *J. Geophys. Res. Solid Earth* 104, 22825–22843. <https://doi.org/10.1029/1999jb900195>.
- Cannat, M., Briais, A., Deplus, C., Escartín, J., Georgen, J., Lin, J., Mercouriev, S., Meyzen, C., Müller, M., Pouliquen, G., Rabain, A., da Silva, P., 1999b. Mid-Atlantic Ridge-Azores hotspot interactions: Along-axis migration of a hotspot-derived event of enhanced magmatism 10 to 4 Ma ago. *Earth Planet. Sci. Lett.* 173, 257–269. [https://doi.org/10.1016/S0012-821X\(99\)00234-4](https://doi.org/10.1016/S0012-821X(99)00234-4).
- Cannat, M., Sauter, D., Mendel, V., Ruellan, E., Okino, K., Escartín, J., Combier, V., Baala, M., 2006. Modes of seafloor generation at a melt-poor ultraslow-spreading ridge. *Geology* 34, 605–608. <https://doi.org/10.1130/G22486.1>.
- Cannat, M., Sauter, D., Bezos, A., Meyzen, C., Humler, E., Le Rigoleur, M., 2008. Spreading rate, spreading obliquity, and melt supply at the ultraslow spreading Southwest Indian Ridge. *Geochem. Geophys. Geosyst.* 9, 1–26. <https://doi.org/10.1029/2007GC001676>.
- Cannat, M., Sauter, D., Lavier, L., Bickert, M., Momoh, E., Leroy, S., 2019. On spreading modes and magma supply at slow and ultraslow mid-ocean ridges. *Earth Planet. Sci. Lett.* 519, 223–233. <https://doi.org/10.1016/j.epsl.2019.05.012>.
- Carbotte, S.M., Smith, D.K., Cannat, M., Klein, E.M., 2015. Tectonic and magmatic segmentation of the Global Ocean Ridge System: A synthesis of observations. *Geological Society Special Publication*. Geological Society of London, pp. 249–295. <https://doi.org/10.1144/SP420.5>.
- Chen, J., Cannat, M., Tao, C., Sauter, D., Munschy, M., 2021. 780 Thousand years of upper-crustal construction at a melt-rich segment of the ultraslow spreading Southwest Indian Ridge 50°28'E. *J. Geophys. Res. Solid Earth* 126. <https://doi.org/10.1029/2021JB022152>.
- Chen, J., Olive, J.A., Cannat, M., 2022. Thermal regime of slow and ultraslow spreading ridges controlled by melt supply and modes of emplacement. *J. Geophys. Res. Solid Earth* 127, e2021JB023715. <https://doi.org/10.1029/2021JB023715>.
- Cochran, J.R., Kurra, G.J., Edwards, M.H., Coakley, B.J., 2003. The Gakkel Ridge: bathymetry, gravity anomalies, and crustal accretion at extremely slow spreading rates. *J. Geophys. Res. Solid Earth* 108, 2116. <https://doi.org/10.1029/2002JB001830>.
- Dannowski, A., Grevemeyer, I., Phipps Morgan, J., Ranero, C.R., Maia, M., Klein, G., 2011. Crustal structure of the propagating TAMMAR ridge segment on the Mid-Atlantic Ridge, 21.5°N. *Geochem. Geophys. Geosyst.* 12, Q07012. <https://doi.org/10.1029/2011GC003534>.
- de Martin, B.J., Reves-Sohn, R.A., Canales, J.P., Humphris, S.E., 2007. Kinematics and geometry of active detachment faulting beneath the Trans-Atlantic geotraverse (TAG) hydrothermal field on the Mid-Atlantic Ridge. *Geology* 35, 711–714. <https://doi.org/10.1130/G23718A.1>.
- Detrick, R.S., Needham, H.D., Renard, V., 1995. Gravity anomalies and crustal thickness variations along the Mid-Atlantic Ridge between 33°N and 40°N. *J. Geophys. Res. Solid Earth* 100, 3767–3787. <https://doi.org/10.1029/94JB02649>.
- Dick, H.B.J., Lin, J., Schouten, H., 2003. An ultraslow-spreading class of ocean ridge. *Nature* 426, 405–412. <https://doi.org/10.1038/nature02128>.
- Escarlin, J., Smith, D.K., Cann, J., Schouten, H., Langmuir, C.H., Escrig, S., 2008. Central role of detachment faults in accretion of slow-spreading oceanic lithosphere. *Nature* 455, 790–794. <https://doi.org/10.1038/nature07333>.

- Georgen, J.E., Lin, J., Dick, H.J.B., 2001. Evidence from gravity anomalies for interactions of the Marion and Bouvet hotspots with the southwest Indian Ridge: effects of transform offsets. *Earth Planet. Sci. Lett.* 187 [https://doi.org/10.1016/S0012-821X\(01\)00293-X](https://doi.org/10.1016/S0012-821X(01)00293-X).
- Grindlay, N.R., Madsen, J.A., Rommevaux-Jestin, C., Slater, J., 1998. A different pattern of ridge segmentation and mantle Bouguer gravity anomalies along the ultra-slow spreading Southwest Indian Ridge ( $15^{\circ}30'E$  to  $25^{\circ}E$ ). *Earth Planet. Sci. Lett.* 161 [https://doi.org/10.1016/s0012-821x\(98\)00154-x](https://doi.org/10.1016/s0012-821x(98)00154-x).
- Hooft, E.E.E., Detrick, R.S., Toomey, D.R., Collins, J.A., Lin, J., 2000. Crustal thickness and structure along three contrasting spreading segments of the Mid-Atlantic Ridge,  $33.5^{\circ}$ – $35^{\circ}N$ . *J. Geophys. Res. Solid Earth* 105, 8205–8226. <https://doi.org/10.1029/1999jb900442>.
- Huang, Y., Tao, C., Liang, J., Liao, S., Wang, Y., Chen, D., Yang, W., Huang, Y., Tao, C., Liang, J., Liao, S., Wang, Y., Chen, D., Yang, W., 2021. Geological characteristics of the Qiaoyue Seamount and associated ultramafic-hosted seafloor hydrothermal system ( $\sim 52.1^{\circ}E$ , Southwest Indian Ridge). *Acta Oceanol. Sin.* 40, 1–10. <https://doi.org/10.1007/s13131-021-1832-0>.
- Jian, H., Chen, Y.J., Singh, S.C., Li, J., Zhao, M., Ruan, A., Qiu, X., 2017. Seismic structure and magmatic construction of crust at the ultraslow-spreading Southwest Indian Ridge at  $50^{\circ}28'E$ . *J. Geophys. Res. Solid Earth* 122, 18–42. <https://doi.org/10.1002/2016JB013377>.
- Kuo, B.Y., Forsyth, D.W., 1988. Gravity anomalies of the ridge-transform system in the South Atlantic between  $31$  and  $34.5^{\circ}S$ : upwelling centers and variations in crustal thickness. *Mar. Geophys. Res. (Dordr.)* 10, 205–232. <https://doi.org/10.1007/BF00310065>.
- Li, J., Jian, H., Chen, Y.J., Singh, S.C., Ruan, A., Qiu, X., Zhao, M., Wang, X., Niu, X., Ni, J., Zhang, J., 2015. Seismic observation of an extremely magmatic accretion at the ultraslow spreading Southwest Indian Ridge. *Geophys. Res. Lett.* 42, 2656–2663. <https://doi.org/10.1002/2014GL062521>.
- Li, H., Tao, C., Yue, X., Baker, E.T., Deng, X., Zhou, J., Wang, Y., Zhang, G., Chen, J., Lü, S., Su, X., 2020. Enhanced hydrothermal activity on an ultraslow-spreading supersegment with a seismically detected melting anomaly. *Mar. Geol.* 430, 106335. <https://doi.org/10.1016/j.margeo.2020.106335>.
- Lin, J., Purdy, G.M., Schouten, H., Semper, J.-C., Zervas, C., 1990. Evidence from gravity data for focused magmatic accretion along the Mid-Atlantic Ridge. *Nature* 344, 627–632. <https://doi.org/10.1038/344627a0>.
- Liu, Z., Buck, W.R., 2020. Global trends of axial relief and faulting at plate spreading centers imply discrete magmatic events. *J. Geophys. Res. Solid Earth* 125. <https://doi.org/10.1029/2020JB019465>.
- Liu, C., Li, J., Tao, C., Fan, Q., Song, J., Luo, Y., Feng, B., 2020. Variations in faulting style of the Southwest Indian Ridge ( $46^{\circ}$ – $53.5^{\circ}E$ ): implications for crustal accretion process at ultraslow-spreading ridges. *Tectonophysics* 790, 228552. <https://doi.org/10.1016/j.tecto.2020.228552>.
- Liu, J., Tao, C., Zhou, Jianping, Shimizu, K., Li, W., Liang, J., Liao, S., Kuritani, T., Deloule, E., Ushikubo, T., Nakagawa, M., Yang, W., Zhang, G., Liu, Y., Zhu, C., Sun, H., Zhou, Jingjun, 2022. Water enrichment in the mid-ocean ridge by recycling of mantle wedge residue. *Earth Planet. Sci. Lett.* 584, 117455. <https://doi.org/10.1016/j.epsl.2022.117455>.
- Magde, L.S., Sparks, D.W., Detrick, R.S., 1997. The relationship between buoyant mantle flow, melt migration, and gravity bull's eyes at the Mid-Atlantic Ridge between  $33^{\circ}N$  and  $35^{\circ}N$ . *Earth Planet. Sci. Lett.* 148 [https://doi.org/10.1016/s0012-821x\(97\)00039-3](https://doi.org/10.1016/s0012-821x(97)00039-3).
- Martinez, F., Hey, R., 2017. Propagating buoyant mantle upwelling on the Reykjanes Ridge. *Earth Planet. Sci. Lett.* 457, 10–22. <https://doi.org/10.1016/j.epsl.2016.09.057>.
- Mendel, V., Sauter, D., Rommevaux-Jestin, C., Patriat, P., Lefebvre, F., Parson, L.M., 2003. Magmatic-tectonic cyclicity at the ultra-slow spreading Southwest Indian Ridge: evidence from variations of axial volcanic ridge morphology and abyssal hills pattern. *Geochem. Geophys. Geosyst.* 4, 9102. <https://doi.org/10.1029/2002GC000417>.
- Michael, P.J., Langmuir, C.H., Dick, H.J.B., Snow, J.E., Goldstein, S.L., Graham, D.W., Lehnert, K., Kurras, G., Jokat, W., Mühe, R., Edmonds, H.N., 2003. Magmatic and amagmatic seafloor generation at the ultraslow-spreading Gakkel ridge, Arctic Ocean. *Nature* 423, 956–961. <https://doi.org/10.1038/nature01704>.
- Minshull, T.A., Muller, M.R., White, R.S., 2006. Crustal structure of the Southwest Indian Ridge at  $66^{\circ}E$ : seismic constraints. *Geophys. J. Int.* 166, 135–147. <https://doi.org/10.1111/j.1365-246X.2006.03001.x>.
- Niu, X., Ruan, A., Li, J., Minshull, T.A., Sauter, D., Wu, Z., Qiu, X., Zhao, M., Chen, Y.J., Singh, S., 2015. Along-axis variation in crustal thickness at the ultraslow spreading Southwest Indian Ridge ( $50^{\circ}E$ ) from a wide-angle seismic experiment. *Geochem. Geophys. Geosyst.* 16, 468–485. <https://doi.org/10.1002/2014GC005645>.
- Parsons, B., Slater, J.G., 1977. An analysis of the variation of ocean floor bathymetry and heat flow with age. *J. Geophys. Res.* 82, 803–827. <https://doi.org/10.1029/jb082i005p00803>.
- Phipps Morgan, J., Chen, Y.J., 1993. Dependence of ridge-axis morphology on magma supply and spreading rate. *Nature* 364, 706–708. <https://doi.org/10.1038/364706a0>.
- Robinson, C.J., Bickle, M.J., Minshull, T.A., White, R.S., Nichols, A.R.L., 2001. Low degree melting under the Southwest Indian Ridge: the roles of mantle temperature, conductive cooling and wet melting. *Earth Planet. Sci. Lett.* 188, 383–398. [https://doi.org/10.1016/S0012-821X\(01\)00329-6](https://doi.org/10.1016/S0012-821X(01)00329-6).
- Sallarès, V., Charvis, P., 2003. Crustal thickness constraints on the geodynamic evolution of the Galapagos Volcanic Province. *Earth Planet. Sci. Lett.* 214, 545–559. [https://doi.org/10.1016/S0012-821X\(03\)00373-X](https://doi.org/10.1016/S0012-821X(03)00373-X).
- Sandwell, D.T., Smith, W.H.F., 2009. Global marine gravity from retracked Geosat and ERS-1 altimetry: ridge segmentation versus spreading rate. *J. Geophys. Res. Solid Earth* 114. <https://doi.org/10.1029/2008JB006008>.
- Sauter, D., Patriat, P., Rommevaux-Jestin, C., Cannat, M., Briais, A., 2001. The Southwest Indian Ridge between  $49^{\circ}15'E$  and  $57^{\circ}E$ : focused accretion and magma redistribution. *Earth Planet. Sci. Lett.* 192, 303–317. [https://doi.org/10.1016/S0012-821X\(01\)00455-1](https://doi.org/10.1016/S0012-821X(01)00455-1).
- Sauter, D., Cannat, M., Meyzen, C., Bezios, A., Patriat, P., Humler, E., Debayle, E., 2009. Propagation of a melting anomaly along the ultraslow Southwest Indian Ridge between  $46^{\circ}E$  and  $52^{\circ}20'E$ : interaction with the Crozet hotspot? *Geophys. J. Int.* 179, 687–699. <https://doi.org/10.1111/j.1365-246X.2009.04308.x>.
- Sauter, D., Cannat, M., Roumèjon, S., Andreani, M., Birot, D., Bronner, A., Brunelli, D., Carlu, D., Delacour, A., Guyader, V., MacLeod, C.J., Manatschal, G., Mendel, V., Ménez, B., Pasini, V., Ruellan, E., Searle, R., 2013. Continuous exhumation of mantle-derived rocks at the Southwest Indian Ridge for 11 million years. *Nat. Geosci.* 6, 314–320. <https://doi.org/10.1038/ngeo1771>.
- Seton, M., Müller, R.D., Zahirovic, S., Williams, S., Wright, N.M., Cannon, J., Whittaker, J., Matthews, K.J., McGirr, R., 2020. A global dataset of present-day oceanic crustal age and seafloor spreading parameters. *Geochem. Geophys. Geosyst.* <https://doi.org/10.1029/2020gc009214>.
- Straume, E.O., Gaina, C., Medvedev, S., Hochmuth, K., Gohl, K., Whittaker, J.M., Abdul Fattah, R., Doornenbal, J.C., Hopper, J.R., 2019. GlobSed: updated total sediment thickness in the world's oceans. *Geochem. Geophys. Geosyst.* 20, 1756–1772. <https://doi.org/10.1029/2018GC008115>.
- Tao, C., Lin, J., Guo, S., Chen, Y.J., Wu, G., Han, X., German, C.R., Yoerger, D.R., Zhou, N., Li, H., Su, X., Zhu, J., 2012. First active hydrothermal vents on an ultraslow-spreading center: Southwest Indian Ridge. *Geology* 40, 47–50. <https://doi.org/10.1130/G32389.1>.
- Thibaud, R., Gente, P., Maia, M., 1998. A systematic analysis of the Mid-Atlantic Ridge morphology and gravity between  $15^{\circ}N$  and  $40^{\circ}N$ : constraints of the thermal structure. *J. Geophys. Res. Solid Earth* 103, 24223–24243. <https://doi.org/10.1029/97jb02934>.
- Tolstoy, M., Harding, A.J., Orcutt, J.A., 1993. Crustal thickness on the Mid-Atlantic Ridge: Bull's-eye gravity anomalies and focused accretion. *Science* 1979 (262), 726–729. <https://doi.org/10.1126/science.262.5134.726>.
- Wang, J., Zhou, H., Salters, V.J.M., Dick, H.J.B., Standish, J.J., Wang, C., 2020. Trace element and isotopic evidence for recycled lithosphere from basalts from  $48$  to  $53^{\circ}E$ , Southwest Indian Ridge. *J. Petrol.* 61. <https://doi.org/10.1093/petrology/egaa068>.
- Weatherall, P., Marks, K.M., Jakobsson, M., Schmitt, T., Tani, S., Arndt, J.E., Rovere, M., Chayes, D., Ferrini, V., Wigley, R., 2015. A new digital bathymetric model of the world's oceans. *Earth Space Sci.* 2, 331–345. <https://doi.org/10.1002/2015EA000107>.
- Wessel, P., Luis, J.F., Uieda, L., Scharroo, R., Wobbe, F., Smith, W.H.F., Tian, D., 2019. The generic mapping tools version 6. *Geochem. Geophys. Geosyst.* 20 <https://doi.org/10.1029/2019GC008515>.
- Wolfe, C.J., Purdy, G.M., Toomey, D.R., Solomon, S.C., 1995. Microearthquake characteristics and crustal velocity structure at  $29^{\circ}N$  on the Mid-Atlantic Ridge: the architecture of a slow spreading segment. *J. Geophys. Res.* 100 <https://doi.org/10.1029/95jb02399>.
- Yang, A.Y., Zhao, T.P., Zhou, M.F., Deng, X.G., 2017. Isotopically enriched N-MORB: a new geochemical signature of off-axis plume-ridge interaction - a case study at  $50^{\circ}28'E$ , Southwest Indian Ridge. *J. Geophys. Res. Solid Earth* 122, 191–213. <https://doi.org/10.1002/2016JB013284>.
- Yu, X., Dick, H.J.B., 2020. Plate-driven micro-hotspots and the evolution of the Dragon Flag melting anomaly, Southwest Indian Ridge. *Earth Planet. Sci. Lett.* 531, 116002. <https://doi.org/10.1016/j.epsl.2019.116002>.
- Yu, Z., Li, J., Niu, X., Rawlinson, N., Ruan, A., Wang, W., Hu, H., Wei, X., Zhang, J., Liang, Y., 2018. Lithospheric structure and tectonic processes constrained by microearthquake activity at the central ultraslow-spreading Southwest Indian Ridge ( $49.2^{\circ}$  to  $50.8^{\circ}E$ ). *J. Geophys. Res. Solid Earth* 123, 6247–6262. <https://doi.org/10.1029/2017JB015367>.
- Zhang, T., Lin, J., Gao, J.Y., 2013. Magmatism and tectonic processes in Area A hydrothermal vent on the Southwest Indian Ridge. *Sci. China Earth Sci.* 56, 2186–2197. <https://doi.org/10.1007/s11430-013-4630-5>.
- Zhang, T., Gao, J., Xu, M., Shen, Z., Wu, Z., 2018. Thickness of extrusive basalts dominating the magnetic structure along the ultraslow-spreading Mohns Ridge axis ( $71.8^{\circ}$ – $73.7^{\circ}N$ ). *Tectonophysics* 742–743. <https://doi.org/10.1016/j.tecto.2018.05.009>.
- Zhao, M., Qiu, X., Li, J., Sauter, D., Ruan, A., Chen, J., Cannat, M., Singh, S., Zhang, J., Wu, Z., Niu, X., 2013. Three-dimensional seismic structure of the Dragon Flag oceanic core complex at the ultraslow-spreading Southwest Indian Ridge ( $49^{\circ}39'E$ ). *Geochem. Geophys. Geosyst.* 14, 4544–4563. <https://doi.org/10.1002/ggpe.20264>.
- Zhou, H., Dick, H.J.B., 2013. Thin crust as evidence for depleted mantle supporting the Marion Rise. *Nature* 494, 195–200. <https://doi.org/10.1038/nature11842>.
- Zhou, F., Dyment, J., Tao, C., Wu, T., 2022. Magmatism at oceanic core complexes on the ultraslow Southwest Indian Ridge: insights from near-seafloor magnetics. *Geology* 50, 726–730. <https://doi.org/10.1130/G49771.1>.